

A small-world of weak ties provides optimal global integration of self-similar modules in functional brain networks

Lazaros K. Gallos and Hernán A. Makse

*Levich Institute and Physics Department,
City College of New York, New York, NY 10031, USA*

Mariano Sigman

*Integrative Neuroscience Laboratory, Physics Department,
FCEyN, Universidad de Buenos Aires, Buenos Aires, Argentina*

Abstract

The human brain is organized in functional modules. Such an organization presents a basic conundrum: modules ought to be sufficiently independent to guarantee functional specialization and sufficiently connected to bind multiple processors for efficient information transfer. It is commonly accepted that small-world architecture of short lengths and large local clustering may solve this problem. However, there is intrinsic tension between shortcuts generating small-worlds and the persistence of modularity; a global property unrelated to local clustering. Here, we present a possible solution to this puzzle. We first show that a modified percolation theory can define a set of hierarchically organized modules made of strong links in functional brain networks. These modules are “large-world” self-similar structures and, therefore, are far from being small-world. However, incorporating weaker ties to the network converts it into a small-world preserving an underlying backbone of well-defined modules. Remarkably, weak ties are precisely organized as predicted by theory maximizing information transfer with minimal wiring cost. This trade-off architecture is reminiscent of the “strength of weak ties” crucial concept of social networks. Such a design suggests a natural solution to the paradox of efficient information flow in the highly modular structure of the brain.

I. INTRODUCTION

One of the main findings in Neuroscience is the modular organization of the brain which in turn implies the parallel nature of brain computations [1–3]. For example, in the visual modality, more than thirty visual areas analyze simultaneously distinct features of the visual scene: motion, color, orientation, space, form, luminance and contrast among others [4]. These features, as well as information from different sensory modalities, have to be integrated, as one of the main aspects of perception is its unitary nature [1, 5].

This leads to a basic conundrum of brain networks: modular processors have to be sufficiently isolated to achieve independent computations, but also globally connected to be integrated in coherent functions [1, 2, 6]. A current view is that small-world networks provide a solution to this puzzle since they combine high local clustering and short path length [7–9]. This view has been fueled by the systematic finding of small-world topology in a wide range of human brain networks derived from structural [10], functional [11–13], and diffusion tensor MRI [14]. Small-world topology has also been identified at the cellular-network scale in functional cortical neuronal circuits in mammals [15, 16] and even in the nervous system of the nematode *Caenorhabditis elegans* [8]. Moreover, small-world property seems to be relevant for brain function since it is affected by disease [17], normal aging and by pharmacological blockade of dopamine neurotransmission [13].

While brain networks show small-world properties, several experimental studies have also shown that they are hierarchical, fractal and highly modular [2, 3, 18, 19]. As there is an intrinsic tension between modular and small-world organization, the main aim of this study is to reconcile these ubiquitous and seemingly contradictory topological properties. Indeed, traditional models of small-world networks cannot fully capture the coexistence of highly modular structure with broad global integration. First, clustering is a purely local quantity which can be assessed inspecting the immediate neighborhood of a node [8]. On the contrary, modularity is a global property of the network, determined by the existence of strongly connected groups of nodes that are only loosely connected to the rest of the network [2, 3, 20, 21]. In fact, it is easy to construct modular and unclustered networks or, reciprocally, clustered networks without modules.

Second, the short distances of a small-world may be incompatible with strong modularity which typically presents the properties of a “large-world” [22–28] characterized by long

distances which effectively suppress diffusion and free flow in the system [27]. While a clustered network preserves its clustering coefficient when a small fraction of shortcuts are added (converting it into a small-world) [8], the persistence of modules is not equally robust. As we show below, shrinking the network diameter may quickly destroy the modules.

Hence, the concept of small-world may not be entirely sufficient to explain the modular and integration features of functional brain networks on its own. We propose that a solution to modularity and broad integration can be achieved by a network in which strong links form large-world fractal modules, in agreement with [2, 3, 18, 19], which are short-cutted by weaker links establishing a small-world network. A modified percolation theory [29, 30] can identify a sequence of critical values of connectivity thresholds forming a hierarchy of modules which progressively merge together. This proposal is inspired by a fundamental notion of sociology termed by Granovetter as “the strength of weak ties” [31, 32]. According to this theory, strong ties (close friends) clump together forming modules. An acquaintance (weak tie) becomes a crucial bridge (a shortcut) between the two densely knit clumps (modules) of close friends [31].

Interestingly, this theme also emerges in theoretical models of large-scale cognitive architecture. Several theories suggest integration mechanisms based on dynamic binding [6, 33] or on a workspace system [1, 34]. For instance, the workspace model [1, 34] proposes that a flexible routing system with dynamic and comparably weaker connections transiently connects modules with very strong connections carved by long-term learning mechanisms.

II. RESULTS

A. Experimental design and network construction

We capitalize on a well-known dual-task paradigm, the psychological refractory period [35]. A total of 16 subjects responded with the right hand to a visual stimulus and with the left hand to an auditory stimulus (see SI Appendix). The temporal gap between the auditory and visual stimuli varied in four stimulus onset asynchrony, SOA= 0, 300, 900 and 1200 ms. The sequence of activated regions which unfolds during the execution of the task has been reported in a previous study [36].

The network analysis relies on the time-resolved BOLD-fMRI response based on the phase

signal obtained for each voxel of data [37]. We first compute the phase of the BOLD signal for each voxel with methods developed previously [37]. For each subject and each SOA task, we obtain the phase signal of the i -th voxel of activity, $\phi_i(t)_{\{t=1,\dots,T\}}$, over $T = 40$ trials performed for a particular SOA value and subject. We use these signals to construct the network topology of brain voxels based on the equal-time cross-correlation matrix, C_{ij} , where a network link indicates a high cross-correlation in the phase activity of the two voxels (see SI Appendix). The accuracy of the calculated C_{ij} values was estimated through a bootstrapping analysis. The 95% confidence interval becomes more narrow for higher C_{ij} values, e.g., for $C_{ij} = 0.975$ it is (0.9744, 0.9760). The corresponding standard deviation is of the order of 0.003. Thus, we typically distinguish between values that differ by 0.005 (see SI Appendix and Fig. S1).

To construct the network, we link two voxels if their cross-correlation C_{ij} is larger than a predefined threshold value p [11, 12, 38]. The resulting network for a given p is a representation of functional relations among voxels for a specific subject and SOA. We obtain 64 cross-correlation networks resulting from the four SOA values presented to the 16 subjects.

B. Percolation analysis

Graph analyses of brain correlations relies on a threshold [11] which is problematic since small-world like properties are sensitive to even a small proportion of variation in the connections. The present analysis may be seen as an attempt to solve this problem.

The thresholding procedure can be naturally mapped to a percolation process (defined in the $N \times N$ space of interactions C_{ij}); a model to describe geometrical phase transitions of connected clusters in random graphs, see Chapters 2 and 3 in [29] and [30, 39].

In general, the size of the largest component of connected nodes in a percolation process remains very small for large p . The crucial concept is that the largest connected component increases rapidly through a critical phase transition at p_c , in which a single incipient cluster dominates and spans the system [29, 30, 39]. A unique connected component is expected to appear if the links in the network are occupied at random without correlations. However, when we apply the percolation analysis to the functional brain network, a more complex picture emerges revealing a hierarchy of clusters arising from the non-trivial correlations in brain activity.

For each participant, we calculate the size of the largest connected component as a function of p . We find that the largest cluster size increases progressively with a series of sharp jumps (Fig. 1A, SOA=900 ms, all participants, other stimuli are similar). This suggests a multiplicity of percolation transitions where percolating modules subsequently merge as p decreases rather than following the typical uncorrelated percolation process with a single spanning cluster. Each of these jumps defines a percolation transition focused on groups of nodes which are highly correlated, constituting well-defined modules.

Figure 1B shows the detailed behavior of the jumps in a typical individual (subject labeled #1 in our dataset [40], SOA=900 ms). At high values of p , three large clusters are formed localized to the medial occipital cortex (red), the lateral occipital cortex (orange) and the anterior cingulate (green). At a lower $p = 0.979$, the orange and red clusters merge as revealed by the first jump in the percolation picture. As p continues to decrease this mechanism of cluster formation and absorption repeats, defining a hierarchical process as depicted in the top panel of Fig. 1B. This analysis further reveals the existence of “stubborn” clusters. For instance, the anterior cingulate cluster (green), known to be involved in cognitive control [41, 42] and which hence cannot commit to a specific functional module, remains detached from the other clusters down to low p values. Even at the lower values of p , when a massive region of the cortex including motor, visual and auditory regions has formed a single incipient cluster (red, $p \approx 0.94$), two new clusters emerge; one involving subcortical structures including the thalamus and striatum (cyan) and the other involving the left frontal cortex (purple). This mechanism reveals the iteration of a process by which modules form at a given p value and merged by comparably weaker links. This process is recursive. The weak links of a given transition become the strong links of the next transition, in a hierarchical fashion.

Here, we focus our analysis on the first jump in the size of the largest connected component, for instance, $p_c = 0.979$ in Fig. 1B. We consider the three largest modules at p_c with at least 1,000 voxels each. This analysis results in a total of 192 modules among all participants and stimuli which are pooled together for the next study. An example of an identified module in the medial occipital cortex of subject #1 and SOA=900 ms is shown in Fig. 1C in the network representation and in Fig. 1D in real space. The topography of the modules reflects coherent patterns across the subjects and stimuli as analyzed in SI Appendix (see Fig. S2).

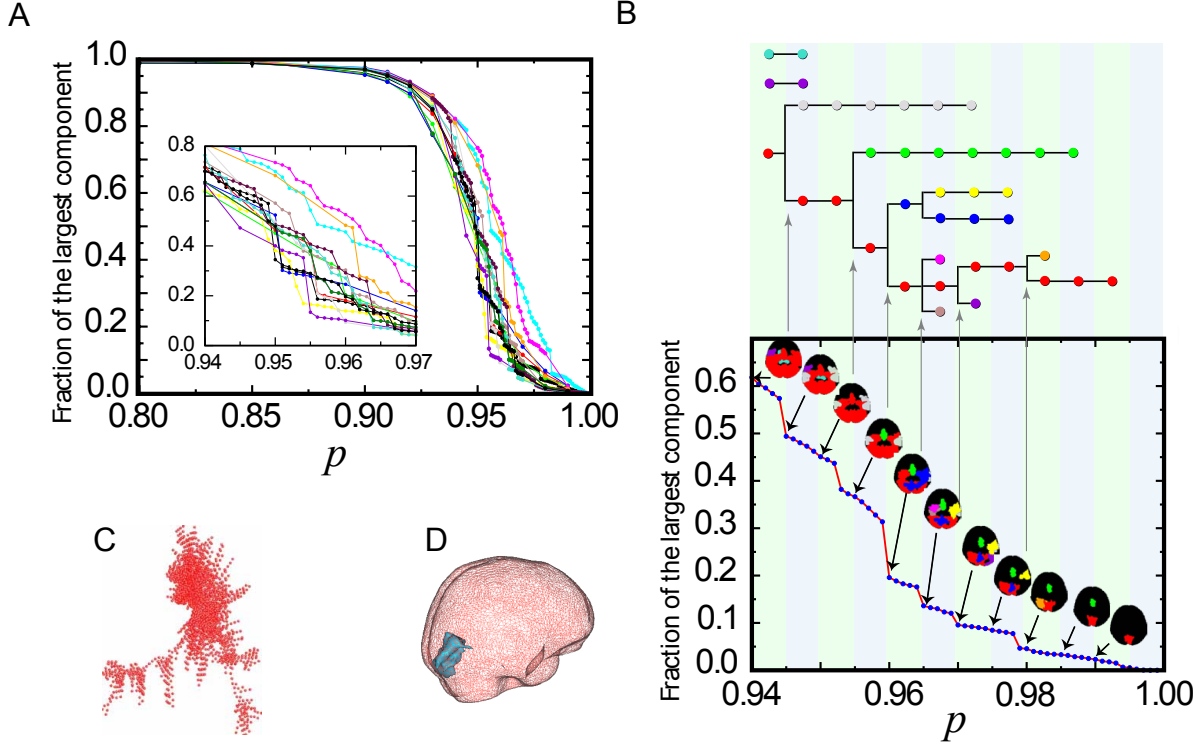


FIG. 1. **Percolation analysis.** (A) Size of the largest connected component of voxels (as measured by the fraction to the total system size) versus p for the 16 subjects (SOA=900 ms). The other three SOA values give similar results. The inset presents a detail around $p \approx 0.95$. (B) Detail for a representative individual. As we lower p the size of the largest component increases in jumps when new modules emerge, grow, and finally get absorbed by the largest component. We show the evolution of the modules by plotting connected components with more than 1,000 voxels. The hierarchical tree at the top of the plot shows how clusters evolve by merging with each other. (C) A typical module in network representation. (D) The same module as in (C) embedded in real space - this specific module projects to the medial occipital cortex, see SI Appendix for the spatial projection of all modules.

C. Scaling analysis and Renormalization Group

To determine the structure of the modules we investigate the scaling of the “mass” of each module (the total number of voxels in the module, N_c) as a function of three length-scales defined for each module: (i) the maximum path length, ℓ_{\max} , (ii) the average path length between two nodes, $\langle \ell \rangle$, and (iii) the maximum Euclidean distance among any two

nodes in the cluster, r_{\max} . The path length, ℓ , is the distance in network space defined as the number of links along the shortest path between two nodes. The maximum ℓ_{\max} is the largest shortest path in the network.

Figure 2A indicates power-law scaling for these quantities [22, 29]. For instance:

$$N_c(r_{\max}) \sim (r_{\max})^{d_f}, \quad (1)$$

defines the Euclidean Hausdorff fractal dimension, $d_f = 2.1 \pm 0.1$. The scaling with ℓ_{\max} and $\langle \ell \rangle$ is consistent with Eq. (1) as seen in Fig. 2A. The exponent d_f quantifies how densely the volume of the brain is covered by a specific module.

Next, we investigate the network properties of each module, applying Renormalization Group (RG) analysis for complex networks [22–26]. This technique allows one to observe the network at different scales transforming it into successively simpler copies of itself, which can be used to detect characteristics which are difficult to identify at a specific scale of observation. We use this technique to characterize sub-modular structure within each brain module [2].

We consider each module identified at p_c separately. We then tile it with the minimum number of boxes or sub-modules, N_B , of a given box diameter ℓ_B [22], i.e., every pair of nodes in a box has shortest path length smaller than ℓ_B . Notice that the calculations are performed in network space, where path lengths are defined across the network links without the need for an embedding dimension.

Covering the network with minimal N_B sub-modules represents an optimization problem which is solved using standard box-covering algorithms, such as the Maximum Excluded Mass Burning algorithm, MEMB, which was introduced in [22, 23, 43] to describe the self similarity of complex networks ranging from the WWW, biological and technical networks (see SI Appendix and Fig. 2B describing MEMB; the code can be downloaded from [40]). The requirement to minimize the number of boxes is important since the resulting boxes are characterized by the proximity between all their nodes and minimization of the links connecting the boxes [27]. Thus, the box-covering algorithm detects boxes/submodules that also tend to maximize modularity.

The repetitive application of box-covering at different values of ℓ_B is a RG transformation [22] that yields a different partition of the brain modules in submodules of varying sizes (Fig. 2B). Figure 2C shows the scaling of N_B versus ℓ_B averaged over all the modules for

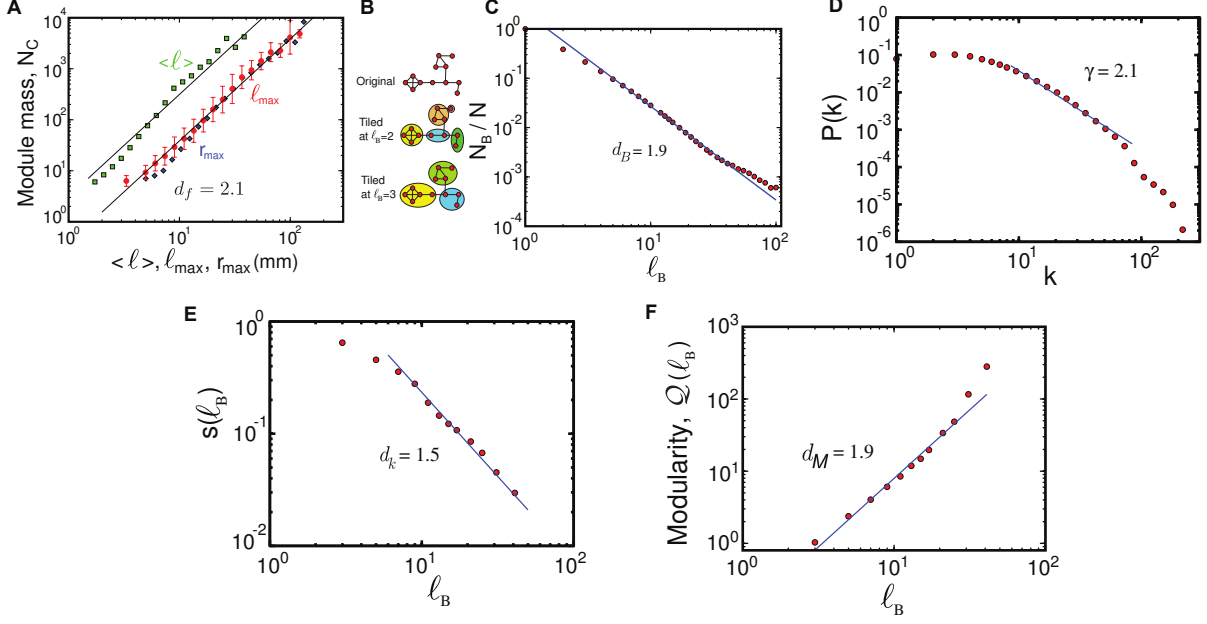


FIG. 2. **Strong ties define fractal modules.** (A) Number of voxels or mass of each module, N_c , versus ℓ_{\max} (red \bullet), $\langle \ell \rangle$ (green \blacksquare), and r_{\max} (blue \blacklozenge). Each point represents a bin average over the modules for all subjects and stimuli. We use all the modules appearing at p_c . The straight lines are fittings according to Eq. (1). The variance is the statistical error over the different modules. The variance is similar in the other data. (B) Detection of submodules and fractal dimension inside the percolation modules. We demonstrate the box-covering algorithm for a schematic network, following the Maximum Excluded Mass Burning algorithm in [22, 43] (SI Appendix). We cover a network with boxes of size ℓ_B which are identified as sub-modules. We define ℓ_B as the shortest path plus one. (C) Scaling of the number of boxes N_B needed to cover the network of a module versus ℓ_B yielding d_B . We average over all the identified modules for all subjects. (D) Degree distribution averaged over all the brain modules. The individual degree distributions for each module (Fig. S4 and SI Appendix) roughly follow a power law with an average exponent $\gamma = 2.11 \pm 0.04$. (E) Dependence of the scaling factor $s(\ell_B)$, defined through $k' = s(\ell_B)k$ for the renormalized degree k' , on ℓ_B . The exponent $d_k = 1.5$ characterizes how the node degree changes during the renormalization process. (F) Quantification of the modularity of the brain modules. The identified percolation modules at p_c are composed of submodules with a high level of modularity as can be seen by the scaling of $Q(\ell_B)$ with ℓ_B that yields a large modularity exponent $d_M = 1.9 \pm 0.1$. Deviations from linear scaling are found at large ℓ_B due to boundary effects since the network is reduced to just a few submodules.

all individuals and stimuli. This property is quantified in the power-law relation [22]:

$$N_B(\ell_B) \sim \ell_B^{-d_B}, \quad (2)$$

where d_B is the box fractal dimension [22–26] which characterizes the self-similarity between different scales of the module where smaller-scale boxes behave in a similar way as the original network. The resulting d_B averaged over all the modules is $d_B = 1.9 \pm 0.1$.

D. Morphology of the brain modules

The RG analysis reveals that the module topology does not have many redundant links and it represents the quantitative statement that the brain modules are “large-worlds”. However this analysis is not sufficient to precisely characterize the topology of the modules. For example, a two-dimensional complex network architecture and a simple two-dimensional lattice are compatible with the scaling analysis and the value of the exponents described in the previous section.

To identify the network architecture of the modules we follow established analysis [18, 44] based on the study of the degree distribution of the modules, $P(k)$, and the degree-degree correlation $P(k_1, k_2)$. The form of $P(k)$ distinguishes between a Euclidean lattice (delta function), an Erdos-Renyi network (Poisson) [30], or a scale-free network (power-law) [44]. We find that the brain modules have a broad degree distribution [11, 44] with an approximate power-law $P(k) \sim k^{-\gamma}$. The statistical analysis provides strong evidence for a power law form and rules out exponential decay (see SI Appendix). In Fig. S4 we present a number of $P(k)$ curves for different modules, along with their best fittings. In the SI Appendix we describe the calculation method that takes into account all the clusters and finally yields an average exponent $\gamma = 2.11 \pm 0.04$. An ‘average’ curve for the distribution is shown in Fig. 2D, where the exponent γ is not a direct fit to this curve, but instead represents the result of the accurate calculation. This result indicates that the modules have a scale-free fractal structure, different from a simple two-dimensional lattice, where $P(k)$ should be a narrow function.

The embedding of scale-free networks in a finite-dimension real space constitutes a problem which has attracted recent attention [45–47]. Scale-free networks may arise from a 2-dimensional lattice with added dense connectivity locally, where the weights and connec-

tivity are inversely proportional to the Euclidean distance on the lattice. To investigate this possibility we study the correlation function of the phases of the voxels as a function of Euclidean distance in real space: $C(r) = \langle \cos(\phi_1 - \phi_2) \rangle$ versus $r = |\vec{r}_1 - \vec{r}_2|$. This function can be interpreted as the correlation between two spins with orientation determined by the phase ϕ_i of the voxel at location \vec{r}_i (average is over all pairs at distance r). We find (see SI Appendix and Fig. S3) that $C(r)$ decays algebraically with distance. Thus, our results indicate that modules are scale-free networks which can be embedded in a lattice with an added long-range connectivity.

How can fractal modularity emerge in light of the scale-free property, which is usually associated with small-worlds [18]? In a previous study [23], we introduced a model to account for the simultaneous emergence of scale-free, fractality and modularity in real networks by a multiplicative process in the growth of the number of links, nodes and distances in the network. The dynamic follows the inverse of the RG transformation [23] where the hubs acquire new connections by linking preferentially with less connected nodes rather than other hubs. This kind of “repulsion between hubs” [24] creates a disassortative structure—with hubs spreading uniformly in the network and not crumpling in the core as in scale-free models [44]. Hubs are buried deep into the modules, while low degree nodes are the intermodule connectors [24].

A signature of such mechanism can be found by following hubs’ degree during the renormalization procedure. At scale ℓ_B , the degree of a hub k changes to the degree of its box k' , through the relation $k' = s(\ell_B)k$. The dependence of the scaling factor $s(\ell_B)$ on ℓ_B defines the renormalized degree exponent d_k by $s(\ell_B) \sim \ell_B^{-d_k}$ [22]. Scaling theory defines precise relations between the exponents for fractal networks [22], through $\gamma = 1 + d_B/d_k$. For the case of brain modules analyzed here (Fig. 2E), we find $d_k = 1.5 \pm 0.1$. Using the values of d_B and d_k for the brain clusters, the prediction is $\gamma = 2.26 \pm 0.11$, which is close to the calculated value of $\gamma = 2.11 \pm 0.04$ from Fig. 2D.

The previous analysis reveals the mechanism of formation of a scale-free network, but it does not assure a fractal topology. Fractality can be determined from the study of the degree-degree correlation through the distribution, $P(k_1, k_2)$ to find a link between nodes with (k_1, k_2) degree. This correlation characterizes the hub-hub repulsion through scaling exponents d_e and ϵ (see SI Appendix and Fig. S5) [23, 48]. In a fractal, they satisfy $\epsilon = 2 + d_e/d_k$. A direct measurement of these exponents yields $d_e = 0.51 \pm 0.08$ and $\epsilon = 2.1 \pm 0.1$

(Fig. S5). Using the measured values of d_e and d_k , we predict $\epsilon = 2.3 \pm 0.1$, which is close to the observed exponent. Taken together, these results indicate a scale-free fractal morphology of brain modules. Such structure is in agreement with previous results of the anatomical connectivity of the brain [2, 3] and functional brain networks [11].

E. Quantifying submodular structure of brain modules

Standard modularity decomposition methods [20, 21] based on maximization of the modularity factor Q as defined in [2, 20, 21, 27, 28] are particularly suitable to uncover the submodular structure. For example, the Girvan-Newman method [20] yields a value of $Q \sim 0.82$ for the brain clusters, indicating a strong modular substructure. The box covering algorithm benefits from detecting submodules (the boxes) at different scales. Then, we can study the hierarchical character of modularity [2, 27, 28], and detect whether modularity is a feature of the network that remains scale-invariant (see SI Appendix and Fig. S6 for a comparison of the submodular structure obtained using Girvan-Newman and box covering).

The minimization of N_B guarantees a network partition with the largest number of intramodule links and the fewest intermodule links. Therefore, the box covering algorithm maximizes the following modularity factor [27, 28]:

$$\mathcal{Q}(\ell_B) \equiv \frac{1}{N_B} \sum_{i=1}^{N_B} \frac{L_i^{\text{in}}}{L_i^{\text{out}}}, \quad (3)$$

which is a variation of the modularity factor, Q , defined in [20, 21]. Here, L_i^{in} and L_i^{out} represent the intra and intermodular links in a submodule i , respectively. Large values of \mathcal{Q} (i.e. $L_i^{\text{out}} \rightarrow 0$) correspond to high modularity [27]. We make the whole modularization method available at [40].

Figure 2F shows the scaling of $\mathcal{Q}(\ell_B)$ averaged over all modules at percolation revealing a monotonic increase with a lack of a characteristic value of ℓ_B . Indeed, the data can be fitted with a power-law form [27]:

$$\mathcal{Q}(\ell_B) \sim \ell_B^{d_M}, \quad (4)$$

which is detected through the modularity exponent, d_M . We study the networks for all the subjects and stimuli and find $d_M = 1.9 \pm 0.1$ (Fig. 2F). The lack of a characteristic length-scale expressed in Eq. (4) implies that submodules are organized within larger modules such

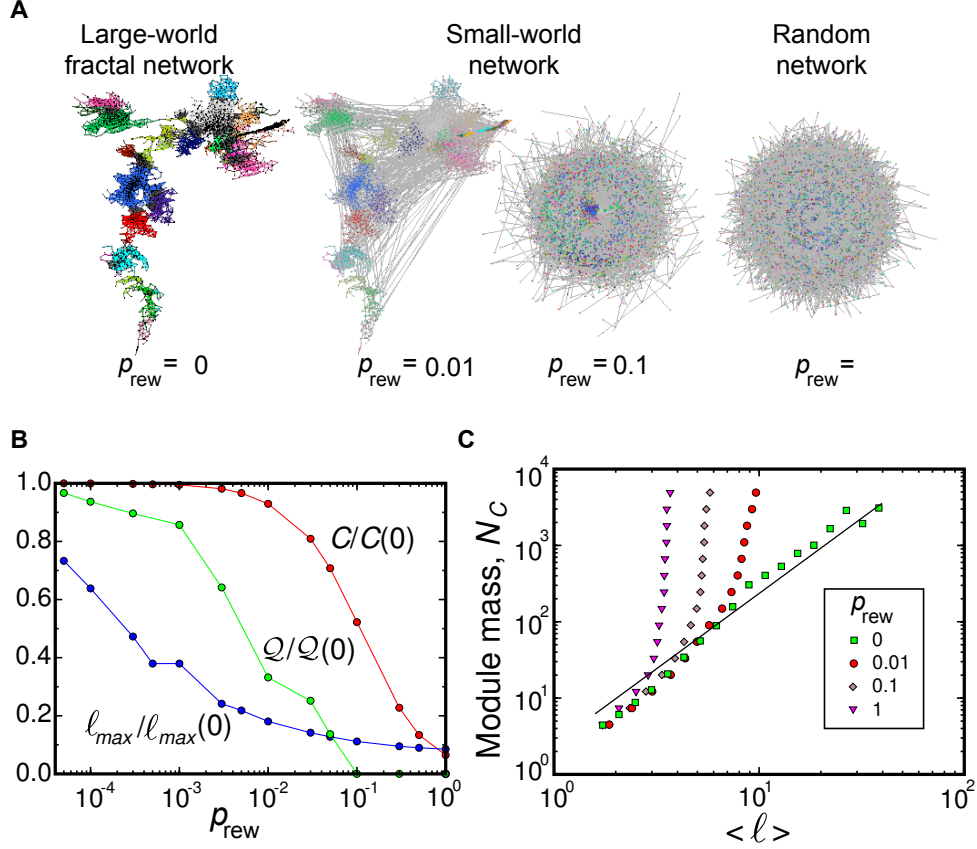


FIG. 3. **Transition from fractal to small-world networks.** (A) Left panel shows a typical percolation module in network space. The colors identify sub-modules obtained by the box-covering algorithm with $\ell_B = 15$. This fractal module contains 4097 nodes with $\langle \ell \rangle = 41.7$, $\ell_{\text{max}} = 139$, and $r_{\text{max}} = 136$ mm. When a small fraction p_{rew} of the links are randomly rewired [8], the modular structure disappears together with the shrinking path length. The rewiring method starts by selecting a random link and cutting one of its edges. This edge is then rewired to another randomly selected node, and another random link starting from this node is selected. This is again cut and rewired to a new random node, and we repeat the process until we have rewired a fraction p_{rew} of links. The final link is then attached to the initially cut node, so that the degree of each node remains unchanged. (B) Small-world cannot coexist with modularity. The large diameter and modularity factor, Eq. (4) for $\ell_B = 15$, of the fractal module in (A) (left panel) diminish rapidly upon rewiring a tiny fraction $p_{\text{rew}} \approx 0.01$ of links, while the clustering coefficient still remains quite large. (C) The transition from fractal to small-world to random structure is shown when we plot the mass versus the average distance for all modules for different p_{rew} values as indicated. The crossover from power-law fractal to exponential small-world/random is shown.

that the inter-connections between those submodules repeat the basic modular character of the entire brain network.

The value of d_M reveals a considerable modularity in the system as it is visually apparent in the sample of Fig. 3A, left panel, where different colors identify the submodules of size $\ell_B = 15$ in a typical fractal module. For comparison, a randomly rewired network (Fig. 3A, right and central panels) shows no modularity and has $d_M \approx 0$. Scaling analysis indicates that d_M is related to $L_{\text{out}} \sim \ell_B^{d_x}$, which defines the outbound exponent d_x characterizing the number of intermodular links for a submodule [27] (d_x is related to the Rent exponent in integrated circuits [3]). From Eq. (4), we find: $d_M = d_B - d_x$, which indicates that the strongest possible modular structure has $d_M = d_B$ ($d_x = 0$) [27]. Such a high modularity induces very slow diffusive processes (subdiffusion) for a random walk in the network [27]. Comparing Eq. (4) with (2), we find $d_x = 0$, which quantifies the maximum degree of modularity in the brain modules.

F. Small-world or large-world fractal modularity

An important consequence of Eqs. (1) and (2) is that the network determined by the strong links above the first p_c -jump lacks the logarithmic scaling characteristic of small-worlds and random networks [8]:

$$\langle \ell \rangle \sim \log N_c, \quad (5)$$

A fractal network poses much larger distances than those appearing in small-worlds [22]: a distance $\ell_{\text{max}} \sim 100$ observed in Fig. 2A (red curve) would require an enormous small-world network $N_c \sim 10^{100}$, rather than $N_c \sim 10^4$, as observed for fractal networks in Fig. 2A. The structural differences between a modular fractal network and a small-world (and a random network) are starkly revealed in the panels of Fig. 3A. We rewire the fractal module on the left panel by randomly reconnecting a fraction p_{rew} of the links while keeping the degree of each node intact [8].

Figure 3B quantifies the transition from fractal ($p_{\text{rew}} = 0$) to small-world ($p_{\text{rew}} \approx 0.01 - 0.1$) and eventually to random networks ($p_{\text{rew}} = 1$), illustrated in Fig. 3A: we plot $\ell_{\text{max}}(p_{\text{rew}})/\ell_{\text{max}}(0)$, the clustering coefficient $C(p_{\text{rew}})/C(0)$ and $\mathcal{Q}(p_{\text{rew}})/\mathcal{Q}(0)$ for a typical $\ell_B = 15$ as we rewire p_{rew} links in the network. As we create a tiny fraction $p_{\text{rew}} = 0.01$ of short-cuts, the topology turns into a collapsed network with no trace of modularity left,

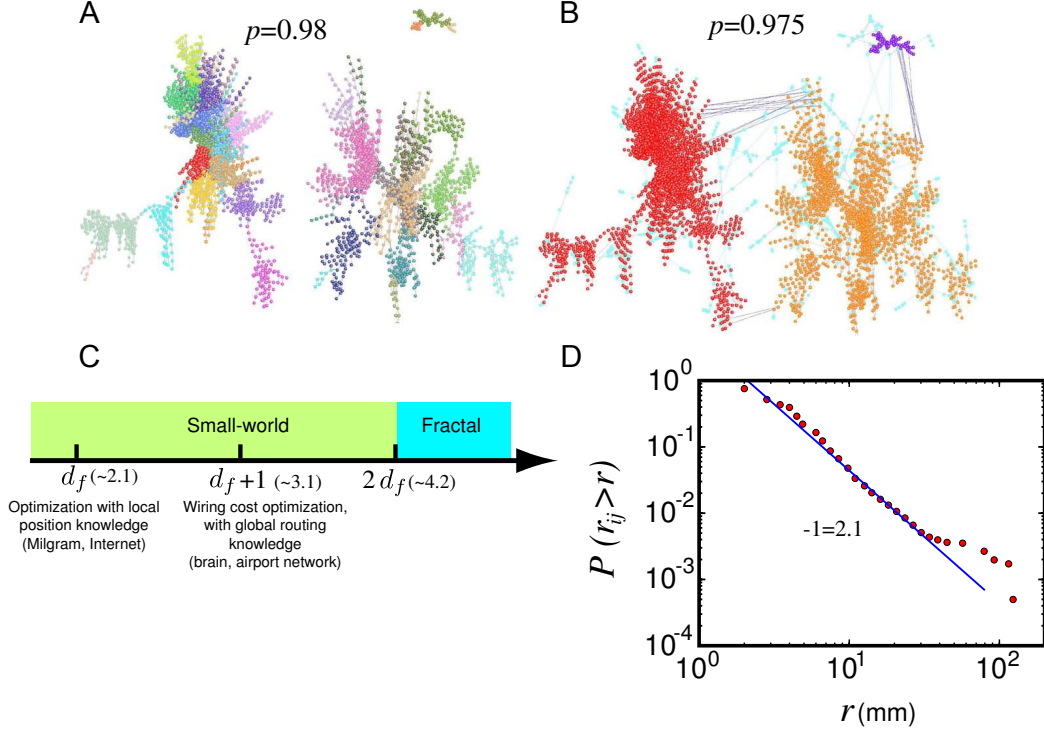


FIG. 4. **Weak ties are optimally distributed.** (A) Three modules identified at $p_c = 0.98$ for the subject in Fig. 1B. The colors correspond to different submodules as identified by the box covering algorithm at $\ell_B = 21$. (B) When we lower the threshold to $p = 0.975$, weak ties connect the modules. The three original modules as they appear in (A) are plotted in red, orange and purple and the light blue nodes are the nodes added from (A) as we lower p . Blue lines represent the added weak links with distance longer than 10 mm. The weak links collapse the three modules into one. (C) Sketch of the different critical values of the shortcut exponent α in comparison with d_f . (D) Cumulative probability distribution $P(r_{ij} > r)$. The straight line fitting yields an exponent $\alpha - 1 = 2.1 \pm 0.1$ indicating optimal information transfer with wiring cost minimization [50]. Certain clusters occupy two diametric parts of the brain. In practice, these are two modules that are connected through long-range links. These links increase significantly the percentage of links at large distances r_{ij} , since they are superimposed on top of the regular distribution of links within unfragmented clusters. This behavior is manifested as a bump in the curve.

while $C(0.01)$ still remains quite high (Fig. 3B). The rewired networks present the exponential behavior of small-worlds [8], and also random networks as p_{rev} increases, obtained

from Eq. (5):

$$N_c \sim \exp(\langle \ell \rangle / \ell_0), \quad (6)$$

where N_c is averaged over all the modules (Fig. 3C). The characteristic size is very small and progressively shrinks to $\ell_0 = 1/7$ when $p_{\text{rew}} = 1$. The hallmark of small-worlds and random networks, exponential scaling Eq. (6), is incompatible with the hallmark of fractal large-worlds, power-law scaling Eq. (2). Similarly, while we find a broad domain where short network distances coexist with high clustering forming a small-world behavior, modularity does not show such a robust behavior to the addition of shortcuts.

G. Short-cut wiring is optimal for efficient flow

Figure 3B suggests that modularity and small-world cannot coexist at the same level of connectivity strength. Next, we set out to investigate how the small-world emerges.

When we extend the percolation analysis lowering further the threshold p below p_c , weaker ties are incorporated to the network connecting the self-similar modules through short-cuts. A typical scenario is depicted in Fig. 4A showing the three largest percolation modules identified just before the first percolation jump in the subject #1 shown in Fig. 1B at $p = 0.98$. For this connectivity strength, the modules are separated and show submodular fractal structure indicated in the colored boxes obtained with box covering. When we lower the threshold to $p = 0.975$, Fig. 4B, the modules are now connected and a global incipient component starts to appear. A second global percolation-like transition appears in the system when the mass of the largest component occupies half of the activated area (see e.g. Fig. 1). For different individuals, global percolation occurs in the interval $p = [0.945, 0.96]$ as indicated in the inset of Fig. 1A.

Our goal is to investigate whether the weak links shortcut the network in an optimal manner. When the cumulative probability distribution to find a Euclidean distance between two connected nodes, r_{ij} , larger than r follows a power-law:

$$P(r_{ij} > r) \sim r^{-\alpha+1}, \quad (7)$$

statistical physics makes precise predictions about optimization schemes for global function as a function of the short-cut exponent α and d_f [26, 49, 50]. Specifically, there are three critical values for α as shown schematically in Fig. 4C. If α is too large then shortcuts will not

be sufficiently long and the network will behave as fractal, equal to the underlying structure. Below a critical value determined by $\alpha < 2d_f$ [26], shortcuts are sufficient to convert the network in a small world. Within this regime there are two significant optimization values:

(i) Wiring cost minimization with full routing information. This considers a network of dimension d_f , over which short-cuts are added to optimize communication, with a wiring cost constraint proportional to the total shortcut length. It is also assumed that coordinates of the network are known, i.e. it is the shortest path that it is being minimized. Under these circumstances, the optimal distribution of shortcuts is $\alpha = d_f + 1$ [50]. This precise scaling is found in the US airport network [51] where a cost limitation applies to maximize profits.

(ii) Decentralized Greedy searches with only local information. This corresponds to the classic Milgram’s “small-world experiment” of decentralized search in social networks [49], where a person has knowledge of local links and of the final destination but not of the intermediate routes. Under these circumstances, which also apply to routing packets in the Internet, the problem corresponds to a greedy search, rather than to optimization of the minimal path. The optimal relation for greedy routing is $\alpha = d_f$ [26, 49].

Hence, the analysis of $P(r_{ij} > r)$ provides information both on the topology of the resulting network and on which transport procedure is optimized. This distribution reveals power-law behavior Eq. (7) with $\alpha = 3.1 \pm 0.1$ when averaged over the modules below p_c (Fig. 4D). Given the value obtained in Eq. (1), $d_f = 2.1$, this implies that the network composed of strong and weak links is small-world ($\alpha < 2d_f$) [26] and optimizes wiring cost with full knowledge of routing information ($\alpha = d_f + 1$) [50].

III. DISCUSSION

The existence of modular organization which become small-world when short-cut by weaker ties is reminiscent of the structure found to bind dissimilar communities in social networks. Granovetter’s work in social sciences [31, 32] proposes the existence of weak ties to coheses well-defined social groups into a large-scale social structure. The observation of such an organization in brain networks suggests that it may be a ubiquitous natural solution to the puzzle of information flow in highly modular structures.

Over the last decades, wire length minimization arguments have been used successfully to explain the architectural organization of brain circuitry [52–56]. Minimizing wire length

is in fact of paramount importance, since about 60% of the cortical volume is taken up by wire (axons and dendrites) [57]. This turns out to optimize conduction rate, posing a strict packing limitation of the amount of wire in cortical circuits [57]. Our finding of a distribution of weak links which minimizes wiring cost is hence in line with a previous literature, consistently showing that neural circuit design is under pressure to minimize wiring length. However, some important nuances of the specific optimization procedure ought to be considered. First, we specifically showed that at the mesoscopic scale, short-cut distribution optimizes wiring cost while maintaining network proximity. This is consistent with the organization of large-scale neural networks in which total wiring can in fact be decreased by about 32% (in 95 primate cortical areas) and up to 48% in the global neuronal network of the nematode *Caenorhabditis elegans* [58]. This extra wiring cost comes from long-range connections which achieve network benefits of shortening the distance between pairs of nodes [58].

Our results are in agreement with this observation, suggesting that simultaneous optimization of network properties and wiring cost might be a relevant principle of brain architecture. In simple words, this topology does not minimize the total wire per-se, simply to connect all the nodes; instead it minimizes the amount of wire required to achieve the goal of shrinking the network to a small-world. A second intriguing aspect of our results, which is not usually highlighted, is that this minimization assumes that broadcasting and routing information are known to each node. How this may be achieved— what aspects of the neural code convey its own routing information— remains an open question in Neuroscience.

BOLD fMRI is an indirect measure of brain activity which relies on multiple vascular and biophysical factors which couple the neural response to the haemodynamic signal [59]. Even if in fMRI research it is always assumed that haemodynamic signals reflect metabolic demand generated by local neuronal activity, recent studies have shown reliable haemodynamic signals that entrains to task structure independently of standard neural predictors of haemodynamics [60]. Hence, our results, as any other fMRI analysis, have to be taken cautiously and may partly reflect the underlying structure of vascular motives. Specifically, the human cortical vascular system has a large number of arterial anastomoses which show a seemingly looking fractal structure in the mm to cm range [61]. Precise measurements of fractality have been reported at the micrometer scales in volumes of the order of a few mm^3 [62, 63], which corresponds to approximately a voxel volume, where branching structure of

microcapilarities then generates fractals. Hence, it is possible that the fractal organization of brain modules is inherited from the vascular system itself.

Although we cannot readily test the influence of the vascular system at a large scale, it is still possible to address this concern at a microscopic scale, by discarding neighboring correlations. Neighboring voxels are expected to carry some shared signal due to spatial autocorrelations from the microvascular network. To assure that our results do not rely on neighbouring correlations which might be particularly spurious, we coarse-grained the original fMRI signal by doubling the lattice spacing, reducing the number of voxels by a factor of 8 and repeat the calculations. The results are consistent with the percolation picture of fractal modules, albeit with an expected lower p_c . Such a renormalized p_c is expected from renormalization theory to change under coarse-graining, while the main results on long-range links, such as the value of the exponents, are insensitive to this type of coarse-graining.

We also investigate whether the map of fractal dimension d_B reflects a meaningful organization based on known facts of functional properties of the cortex and the specific task which subjects are performing. We found a topographical organization of fractality in the human brain (Fig. S7). The right portion of the anterior cingulate, SMA and the right PPC regions involved in routing of information and cognitive control [41, 42], which are expected to have a more complex functional organization, are the clusters with higher fractal dimension. The left-right asymmetry is interesting since, in this specific task, the left hand response is queued for a few hundred milliseconds and has to be temporally connected to working memory and inhibitory circuits. While not fully conclusive, this analysis suggests a functional role of the network architectures described here.

Another similar concern is that the recovered brain modules may be a manifestation of the fractal structure of the underlying three-dimensional vortex grid or of the cortex. However, since the dimensions of the grid ($d = 3$) and of the cortex ($d = 2.7$)[64] are both sufficiently different from 1.9 and the connectivity distribution of the modules is much broader than the typical Euclidean fractal cortex (which should be narrow around $k \sim 6$) or a 3d lattice ($k = 6$), we may safely assume that these objects have their own structure. Moreover, we also observed modules with similar fractal dimension in subcortical structures suggesting that these results do not simply reflect anatomical properties of the cortical mantle.

A hierarchical modular organization of the brain composed of modules within modules has been invoked in [2, 3] to describe the brain structure. The present results sup-

port these previous findings, while, at the same time, provide a new view by integrating the results with the (non-critical) properties of small-worlds and placing self-similarity in the framework of scaling theory, universality and Renormalization Groups [65]. In this framework, brain modules are characterized by a set of novel scaling exponents, the septuplet: $(d_f, d_B, d_k, d_e, d_M, \gamma, \alpha) = (2.1, 1.9, 1.5, 0.5, 1.9, 2.1, 3.1)$, and the scaling relations $d_M = d_B - d_x$, relating fractality with modularity, $\alpha = d_f + 1$, relating global integration with modularity, $\gamma = 1 + d_B/d_k$, relating scale-free with fractality, and $\epsilon = 2 + d_e/d_k$, relating degree correlations with fractality.

One advantage of this formalism is that the different brain topologies can be classified into universality classes under RG [65] according to the septuplet $(d_f, d_B, d_k, d_e, d_M, \gamma, \alpha)$. Universality applies to the critical exponents but not to quantities like (p_c, C, ℓ_0) which are sensitive to the microscopic details of the different experimental situations [65]. In this framework, (non-critical) small-worlds are obtained in the limit $(d_f, d_B, d_k, d_e, d_M, d_x) \rightarrow (\infty, \infty, \infty, 0, 0, \infty)$. A path for future research will be to test the universality of the septuplet of exponents under different activities covering other areas of the brain, e.g., the resting-state correlation structure [66].

In conclusion, we propose a formal solution to the problem of information transfer in the highly modular structure of the brain. The answer is inspired by a classic finding in sociology: the strength of weak ties [31]. The present work provides a general insight into the physical mechanisms of network information processing at large. It builds up on an example of considerable relevance to natural science, the organization of the brain, to establish a concrete solution to a broad problem in network science. The results can be readily applied to other systems—where the coexistence of modular specialization and global integration is crucial—ranging from metabolic, protein and genetic networks to social networks and the Internet.

ACKNOWLEDGMENTS

LKG and HAM thank the NSF-0827508 Emerging Frontiers Program for financial support. MS is supported by a Human Frontiers Science Program Fellowship. We thank D.

Bansal, S. Dehaene, S. Havlin, and H.D. Rozenfeld for valuable discussions.

- [1] Dehaene S, Naccache L (2001) Towards a cognitive neuroscience of consciousness: basic evidence and a workspace framework. *Cognition* **79**:1-37.
- [2] Meunier D, Lambiotte R, Bullmore ET (2010) Modular and hierarchically modular organization of brain networks. *Front. Neurosci.* **4**:200.
- [3] Bassett DS, et al. (2010) Efficient physical embedding of topologically complex information processing networks in brains and computer circuits. *PLoS Comput. Biol.* **6**:e1000748.
- [4] Felleman DJ, van Essen DC (1991) Distributed hierarchical processing in the primate cerebral cortex. *Cereb. Cortex* **1**:1-47.
- [5] Treisman A (1996) The binding problem. *Current opinion in neurobiology* **6**:171-178.
- [6] Tononi G, Sporns O, Edelman GM (1994) A measure for brain complexity: relating functional segregation and integration in the nervous system. *Proc. Nat. Acad. Sci. USA* **91**:5033-5037.
- [7] Sporns O, Chialvo DR, Kaiser M, Hilgetag CC (2004) Organization, development and function of complex brain networks. *Trends Cognit. Sci.* **8**:418-425.
- [8] Watts D, Strogatz S (1998) Collective dynamics of 'small-world' networks. *Nature* **393**:440-442.
- [9] Bassett DS, Bullmore ET (2006) Small-world brain networks. *Neuroscientist* **12**:512-523.
- [10] He Y, Chen ZJ, Evans AC (2007) Small-world anatomical networks in the human brain revealed by cortical thickness from MRI. *Cereb. Cortex* **17**:2407-2419.
- [11] Eguiluz VM, Chialvo DR, Cecchi GA, Baliki M, Apkarian AV (2005) Scale-free brain functional networks. *Phys. Rev. Lett.* **94**:018102.
- [12] Achard S, Salvador R, Whitcher B, Suckling J, Bullmore ET (2006) A resilient, low-frequency, small-world human brain functional network with highly connected association cortical hubs. *J. Neurosci.* **26**:63-72.
- [13] Achard S, Bullmore ET (2007) Efficiency and cost of economical brain functional networks. *PLoS Comput. Biol.* **3**:e17.
- [14] Hagmann P, et al. (2007) Mapping human whole-brain structural networks with diffusion MRI. *PLoS One* **2**:e597.
- [15] Song S, Sjostrom PJ, Reigl M, Nelson S, Chklovskii DB (2005) Highly nonrandom features of

- synaptic connectivity in local cortical circuits. *PLoS Biol.* **3**:e68.
- [16] Yu S, Huang D, Singer W, Nikolic D (2008) A small world of neuronal synchrony. *Cereb. Cortex* **18**:2891-2901.
 - [17] Stam CJ, Jones BF, Nolte G, Breakspear M, Scheltens P (2007) Small-world networks and functional connectivity in Alzheimer's disease. *Cereb. Cortex* **17**:92-99.
 - [18] Ravasz E, Somera AL, Mongru DA, Oltvai ZN, Barabási A-L (2002) Hierarchical organization of modularity in metabolic networks. *Science* **297**:1551-1555.
 - [19] Palla G, Derenyi I, Farkas I, Vicsek T (2005) Uncovering the overlapping community structure of complex networks in nature and society. *Nature* **435**:814-818.
 - [20] Girvan M, Newman MEJ (2002) Community structure in social and biological networks. *Proc. Nat. Acad. Sci.* **99**:7821-7826.
 - [21] Fortunato S (2010) Community detection in graphs. *Phys. Rep.* **486**:75-174.
 - [22] Song C, Havlin S, Makse HA (2005) Self-similarity of complex networks. *Nature* **433**:392-395.
 - [23] Song C, Havlin S, Makse HA (2006) Origins of fractality in the growth of complex networks. *Nature Phys.* **2**:275-281.
 - [24] Goh KI, Salvi G, Kahng B, Kim D (2006) Skeleton and fractal scaling in complex networks. *Phys. Rev. Lett.* **96**:018701.
 - [25] Radicchi F, Ramasco JJ, Barrat A, Fortunato S (2008) Complex networks renormalization: flows and fixed points. *Phys. Rev. Lett.* **101**:148701.
 - [26] Rozenfeld HD, Song C, Makse HA (2010) The small world-fractal transition in complex networks: A renormalization group approach. *Phys. Rev. Lett.* **104**:025701.
 - [27] Gallos LK, Song C, Havlin S, Makse HA (2007) Scaling theory of transport in complex biological networks. *Proc. Nat. Acad. Sci. USA* **104**:7746-7751.
 - [28] Galvao V, et al. (2010) Modularity map of the human cell differentiation network. *Proc. Nat. Acad. Sci. USA* **107**:5750-5755.
 - [29] Bunde A, Havlin S, editors (1996) *Fractals and Disordered Systems* 2nd edition (Springer-Verlag, Heidelberg).
 - [30] Bollobás B (1985) *Random Graphs* (Academic Press, London).
 - [31] Granovetter MS (1973) The strength of weak ties. *American Journal of Sociology* **78**:1360-1380.
 - [32] Onnela J-P, et al. (2007) Structure and tie strengths in mobile communication networks. *Proc.*

- Nat. Acad. Sci. USA* **104**:7332-7336.
- [33] Tononi G, Edelman GM (1998) Consciousness and complexity. *Science* **282**:1846-1851.
 - [34] Baars BJ (1997) In the theater of consciousness: The workspace of the mind. (Oxford University Press, USA).
 - [35] Pashler H (1994) Dual-task interference in simple tasks: Data and theory. *Psychological Bulletin* **116**:220-220.
 - [36] Sigman M, Dehaene S (2008) Brain mechanisms of serial and parallel processing during dual-task performance. *J. Neurosci.* **28**:7585-7598.
 - [37] Sigman M, Jobert A, Dehaene S (2007) Parsing a sequence of brain activations of psychological times using fMRI. *Neuroimage* **35**:655-668.
 - [38] Salvador R, et al. (2005) Neurophysiological architecture of functional magnetic resonance images of human brain. *Cereb. Cortex* **15**:1332-1342.
 - [39] Stanley HE (1971) *Introduction to phase transitions and critical phenomena*. (Oxford University Press, Oxford).
 - [40] The entire experimental dataset and modularization and fractal codes are available at <http://lev.ccny.cuny.edu/~hmake/brain.html>
 - [41] Zylberberg A, Dehaene S, Roelfsema PR and Sigman M (2011) The human Turing machine: a neural framework for mental programs. *Trends in Cognitive Sciences* **15**: 293-300.
 - [42] Duncan, J (2010) The multiple-demand (MD) system of the primate brain: mental programs for intelligent behaviour. *Trends in Cognitive Sciences* **14**:172-179.
 - [43] Song C, Gallos LK, Havlin S, Makse HA (2007) How to calculate the fractal dimension of a complex network: the box covering algorithm. *J. Stat. Mech.* P03006.
 - [44] Barabási A-L, Albert R (1999) Emergence of scaling in random networks. *Science* **286**:509-512.
 - [45] De Arcangelis L, Herrmann HJ (2010) Learning as a phenomenon occurring in a critical state. *Proc. Nat. Acad. Sci. USA* **107**:3977-3981.
 - [46] Li D, Li G, Kosmidis K, Stanley HE, Bunde A, Havlin S (2011) Percolation of spatially constraint networks. *Euro. Phys. Lett.* **93**:68004.
 - [47] Daqing L, Kosmidis K, Bunde A, Havlin S (2011) Dimension of spatially embedded networks. *Nature Phys.* **7**: 481-484.
 - [48] Gallos LK, Song C, Makse HA (2008) Scaling of degree correlations and its Influence on diffusion in scale-free networks, *Phys. Rev. Lett.* **100**:248701.

- [49] Kleinberg J (2000) Navigation in a small world. *Nature* **406**:845.
- [50] Li G, Reis SDS, Moreira AA, Havlin S, Stanley HE, Andrade Jr JS (2010) Towards design principles for optimal transport networks. *Phys. Rev. Lett.* **104**:018701.
- [51] Bianconi G, Pin P, Marsili M (2009) Assessing the relevance of node features for network structure. *Proc. Nat. Acad. Sci. USA* **106**:11433-11438.
- [52] Cowey A (1979) Cortical maps and visual perception: The Grindley Memorial Lecture. *The Quarterly Journal of Experimental Psychology*, **31**:1-17.
- [53] Linsker R (1986) From basic network principles to neural architecture: emergence of spatial-opponent cells. *Proceedings of the National Academy of Sciences* **83**:7508.
- [54] Mitchison G (1991) Neuronal branching patterns and the economy of cortical wiring. *Proceedings of the Royal Society of London B* **245**:151.
- [55] Cherniak C (1995) Neural component placement. *Trends in neuroscience* **18**:522-527.
- [56] Chklovskii DB (2000) Optimal sizes of dendritic and axonal arbors in a topographic projection. *Journal of neurophysiology* **83**:2113.
- [57] Chklovskii DB, Schikorski, T and Stevens, CF (2002) Wiring optimization in cortical circuits *Neuron* **34**: 341–347
- [58] Kaiser M, Hilgetag CC (2006) Nonoptimal component placement, but short processing paths due to long-distance projections in neural systems. *PLoS Comput. Biol.* **2**:e95.
- [59] Logothetis NK, Pauls J, Augath M, Trinath T, and Oeltermann A (2001) Neurophysiological investigation of the basis of the fMRI signal. *Nature* **412**:150-157.
- [60] Sirotin YB and Das A (2009) Anticipatory haemodynamic signals in sensory cortex not predicted by local neuronal activity. *Nature* **457**:475-479.
- [61] Duvernoy HM, Delon S and Vannson JL (1981) AnticipCortical blood vessels of the human brain. *Brain Research Bulletin* **7**:519-579.
- [62] Cassot F, Lauwers F, Fouard C, Prohaska S, and Lauwers-Cances V (2006) A novel three-dimensional computer-assisted method for a quantitative study of microvascular networks of the human cerebral cortex. *Microcirculation* **13**:1-18.
- [63] Risser L, Plouraboué F, Steyer A, Cloetens P, Le Duc G, and Fonta C (2006) From homogeneous to fractal normal and tumorous microvascular networks in the brain. *Journal of Cerebral Blood Flow & Metabolism* **27**:293-303.
- [64] Kiselev VG, Hahn KR, Auer DP (2003) Is the brain cortex a fractal? *NeuroImage* **20**:1765-

1774.

- [65] Stanley HE (1999) Scaling, universality, and renormalization: Three pillars of modern critical phenomena. *Rev. Mod. Phys.* **71**:S358-S366.
- [66] Raichle ME, et al. (2001) A default mode of brain function. *Proc. Natl. Acad. Sci. USA* **98**:676-682.

SUPPORTING INFORMATION

I. FMRI METHODS AND NETWORK CONSTRUCTION

A total of 16 participants (7 women and 9 men, mean age, 23, ranging from 20 to 28) were asked to perform two tasks with the instruction that they had to respond accurately and fast to each of them. The first task was a visual task of comparing a given number (target T1) to a fixed reference, and, second, an auditory task of judging the pitch of an auditory tone (target T2) [36]. The two stimuli are presented with a stimulus onset asynchrony (SOA), i.e., the delay in the onset of T1 and T2, varying from: SOA=0, 300, 900 and 1200 ms. In the number-comparison task, a number varying randomly among four values (28, 37, 53, 62) was flashed on a computer screen and subjects had to respond, with a key press using the right hand, whether the number was larger or smaller than 45. In the auditory task, subjects had to respond whether the tone was high or low frequency with a key press using the left hand. Full details and preliminary statistical analysis of this experiment have been reported in [36]. The study is part of a larger neuroimaging research program headed by Denis Le Bihan and approved by the Comité Consultatif pour la Protection des Personnes dans la Recherche Biomédicale, Hôpital de Bicêtre (Le Kremlin-Bicêtre, France).

Subjects performed a total of 160 trials (40 for each SOA value) with a 12 s inter-trial interval [37]. The 160 trials were performed in five blocks of 384 s with a resting time of \sim 5 min between blocks. For each trial, we recorded whole-brain fMRI images at a sampling time, TR = 1.5 s producing 8 fMRI images between two consecutive trials. From these images we computed the phase and amplitude of the hemodynamic response of each trial as explained in [37]. The experiments were performed on a 3T fMRI system (Bruker). Functional images sensitive to blood oxygenation level dependent (BOLD) contrast were obtained with a T2*-weighted gradient echoplanar imaging sequence [repetition time (TR) = 1.5 s; echo time = 40 ms; angle = 90°; field of view (FOV) = 192×256 mm; matrix = 64×64]. The whole brain was acquired in 24 slices with a slice thickness of 5 mm. High-resolution images (three-dimensional gradient echo inversion-recovery sequence, inversion time = 700 ms; FOV = $192 \times 256 \times 256$ mm; matrix = $256 \times 128 \times 256$; slice thickness = 1 mm) were also acquired.

To estimate the periodicity and phase of the event-related BOLD response, the data from

each subject were submitted to a first-level model in which the signal from each trial (8 TRs of 1.5 s) was fitted with three regressors: a constant, a sine, and a cosine function at the above period. To facilitate intersubject averaging across possible differences in anatomical localization, the regression weights of the sines and cosines were stereotactically transformed to the standardized coordinate space of Talairach and Tournoux ([Montreal Neurological Institute] MNI 152 average brain) to spatially normalize for individual differences in brain morphology. Normalized images had a resolution of 8 mm³. Normalized phase images were transformed with the inverse tangent function to yield a phase lag expressed in radians for each voxel i and each trial $t = 1, \dots, T$ over $T = 40$ trials: $\phi_i(t) \in [0, 2\pi]$ [37], indicating phase lags in the interval $[0, 12]$ s.

We calculate cross-correlations between different brain areas based on these phases [11, 12, 38]. We determine the equal-time cross-correlation matrix \mathbb{C} with elements C_{ij} measuring the cross-correlation between the phase activity $\phi_i(t)$ of the i -th and j -th voxel over $T = 40$ trials for each subject and SOA condition:

$$C_{ij} = \frac{1}{T} \sum_{t=1}^T \cos(\phi_i(t) - \phi_j(t)). \quad (8)$$

By construction, the elements satisfy $-1 \leq C_{ij} \leq 1$, where $C_{ij} = 1$ corresponds to perfect correlations, $C_{ij} = -1$ corresponds to perfect anticorrelations, and $C_{ij} = 0$ describes a pair of uncorrelated voxels. The entire experimental dataset is available in [40].

For our analysis, we create a mask where we keep voxels which were activated in more than 75% of the cases, i.e., in at least 48 instances out of the 64 total cases considered. The obtained number of activated voxels is $N \approx 60,000$, varying slightly for different individuals and stimuli. The ‘activated or functional map’ exhibits phases consistently falling within the expected response latency for a task-induced activation [36]. As expected for an experiment involving visual and auditory stimuli and bi-manual responses, the responsive regions included bilateral visual occipito-temporal cortices, bilateral auditory cortices, motor, premotor and cerebellar cortices, and a large-scale bilateral parieto-frontal structure, see SI-Section “Spatial projection of the modules” below. In the present analysis, we do not explore the differences in networks between different conditions. Rather, we consider them as independent experiments, generating a total of 64 different networks, one for each condition of temporal gap and subject.

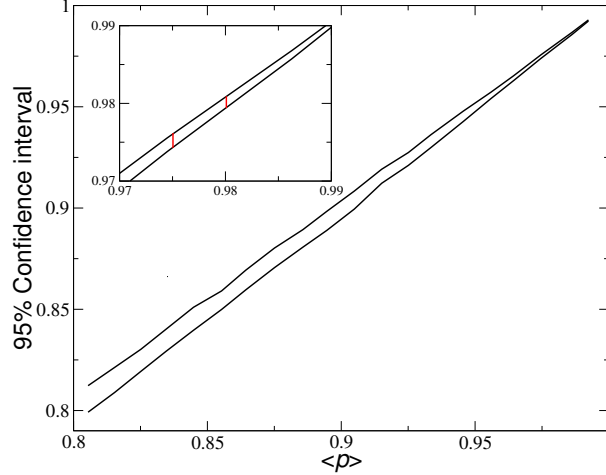


FIG. S1. **Boot strap analysis.** The interval between the two curves corresponds to the 95% confidence interval for the calculation of the mean fraction of links $\langle p \rangle$ as a function of $\langle p \rangle$. The inset zooms in the regime around the values used in Fig. 4A.

The use of fMRI neighboring voxels can be expected to carry some shared signal due to spatial autocorrelations (vascular, subject motion or scanner noise), which could give rise to spurious correlations over short distance. To test for this effect, we double the lattice spacing, reducing the voxels by a factor of 8 and repeat the calculations. The results are consistent with the percolation picture of Fig. 1, albeit with a lower p_c , while the main results on long-range links are insensitive to this type of artifacts.

II. BOOT STRAP ANALYSIS

In order to estimate the accuracy of the correlation calculations, we performed a non-parametric boot strap analysis. We consider the set of the 40 trials per subject and SOA value. We perform the boot strap analysis for each possible pair of voxels. The correlation between two voxels for each of those trials serves as our original sample of 40 correlation values. We then draw 10000 re-samples from this sample with substitution. The arithmetic mean is calculated for each re-sample. Calculating the average value of all these means gives the boot strap estimate for the mean correlation. The 95% boot strap confidence interval is calculated by the distribution of the 10000 mean values at the 0.05 and 0.95 points of the distribution, respectively.

The above process yields the confidence interval for the correlation value between two

voxels. A different pair of voxels may have very different value of correlation, so in Fig. S1 we present the 95% bootstrap confidence interval as a function of the average value of correlation. The interval becomes smaller, i.e. the accuracy of the calculation increases, for larger p values. Considering the networks of Fig. 4A and B, for example, the intervals for $p = 0.975$ and $p = 0.98$ correspond to (see inset) $[0.9744, 0.9760]$ and $[0.9795, 0.981]$, respectively.

III. SPATIAL PROJECTION OF THE MODULES

The complex network representation reveals functional links between brain areas, but cannot directly reveal spatial correlations. Since voxels are embedded in real space, we also study the topological features of modules in three dimensions, where now voxels assume their known positions in the brain and links between them are transferred from the corresponding network, i.e., they are assigned according to the degree of correlation between any two voxels, Eq. (8), which is independent of the voxels proximity in real space. The above procedure yields a different spatial projection of the modules for each subject; an example for subject #1 and SOA=900 ms in the medial occipital cortex is shown in Fig. 1D. We study each of these percolation modules separately and find that they all carry statistically similar patterns. The topography of the identified modules reflects coherent patterns across different subjects, as shown next.

Fig. S2A shows a medial sagittal view of the largest four percolation modules for all the participants under stimulus SOA=0. In virtually all subjects we observe a module covering the anterior cingulate (AC) region, a module covering the medial part of the posterior parietal cortex (PPC) and a module covering the medial part of posterior occipital cortex (area V1/V2), along the calcarine fissure.

We measure the likelihood that a voxel appears in the largest percolation module among all the participants in Fig. S2A by counting, for each voxel, the number of individuals for which it was included in one of the first four percolation modules. The spatial distribution of the first percolation modules averaged over all the subjects depicted in Figs. S2B and S2C shows that modules in the three main modes, V1/V2, AC and PPC, are ubiquitously present in percolation modules and, to a lesser extent, voxels in the motor cortex (along the central sulcus) are slightly more predominantly on the left hemisphere. The correlation

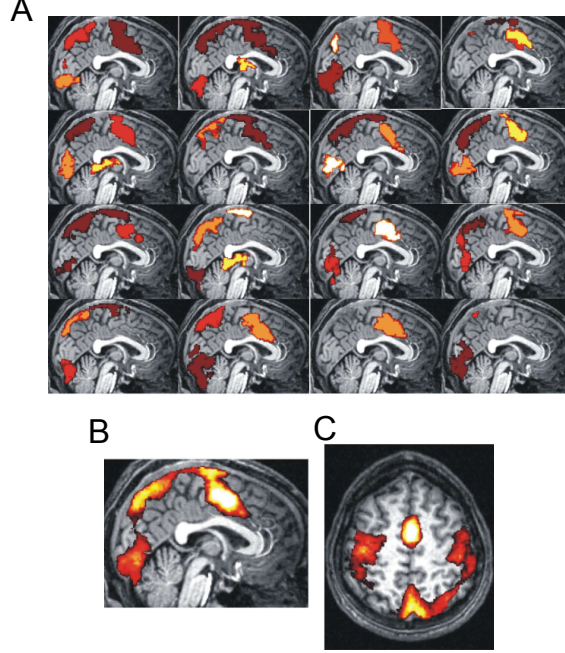


FIG. S2. **The emerging modules have consistent spatial projections.** (A) Spatial distribution of the four largest percolation modules (yellow, orange, red, brown) appearing at the first percolation jump, p_c , for each subject under stimulus SOA=0. Most modules are localized in the same regions: anterior cingulate, posterior medial-occipital, posterior parietal and thalamus. (B) and (C) These panels show the number of times that the largest percolation cluster for each of the 16 subjects appears in a given voxel. White bleached regions correspond to voxels which are active in the 16 subjects, while the red regions correspond to voxels shared by half of the subjects. The anterior cingulate, a fundamental node in cognitive control, is the only region shared by all subjects.

networks obtained from each subject yield modules with consistent topographic projections.

IV. BOX COVERING ALGORITHM FOR FRACTAL DIMENSION IN NETWORK SPACE

For a given percolation module, the detection of submodules or boxes follows from the application of the box-covering algorithm for self-similar networks [22,43]. The algorithm can be downloaded at [40]. In box covering we assign every node to a box or submodule, by finding the minimum possible number of boxes, $N_B(\ell_B)$, that cover the network and whose

diameter (defined as the maximum distance between any two nodes in this box) is smaller than ℓ_B .

We implement the Maximum Excluded Mass Burning (MEMB) algorithm from [43] for box covering. The algorithm uses the basic idea of box optimization, where we require that each box should cover the maximum possible number of nodes, and works as follows: We first locate the optimal ‘central’ nodes which will act as the origins for the boxes. This is done by first calculating the number of nodes (called the mass) within a distance r_B from each node. We use, $\ell_B = 2r_B + 1$. The node that yields the largest mass is marked as a center. Then we mark all the nodes in the box of this center node as ‘tagged’. We repeat the process of calculating the mass of the boxes starting from all non-center nodes, and we identify a second center according to the largest remaining mass, while nodes in the corresponding box are ‘tagged’, and so on. When all nodes are either centers or ‘tagged’ we have identified the minimum number of centers that can cover the network at the given r_B value. Starting from these centers as box origins, we then simultaneously burn the boxes from each origin until the entire network is covered, i.e. each node is assigned to one box (we call this process burning since it is similar to burning algorithms developed to investigate clustering statistics in percolation theory [29,30]). In Fig. 2A we show how box-covering works for a simple network at different ℓ_B values. RG is then the iterative application of this covering at different ℓ_B .

V. CORRELATION FUNCTION

Connections between voxels are determined according to the value of the correlation between the two voxels, as described above. This value may also depend on the physical (Euclidean) distance between the two voxels, since areas that are close to each other should interact stronger.

We studied the correlation function, $C(r)$ of the phases of the voxels:

$$C(r) = \langle \cos(\phi_1 - \phi_2) \rangle, \quad (9)$$

where ϕ_i denotes the phase of voxel i . The distance r is the Euclidean distance between the two voxels 1 and 2 and the average is taken over all pairs at distance r . This function can be interpreted as the correlation between two spins with orientation determined by the phases

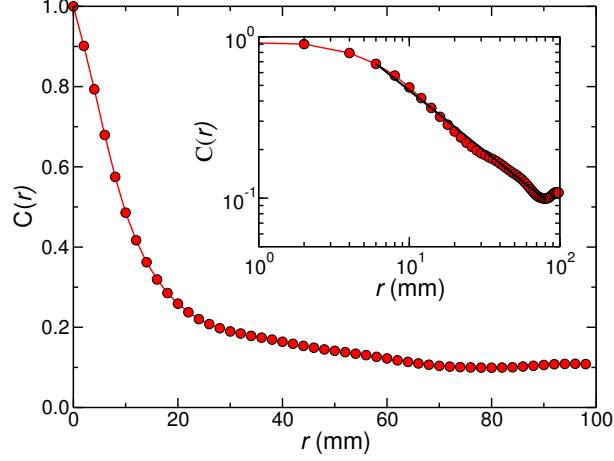


FIG. S3. **Spatial correlation function.** This function measures the correlation $C(r)$ between the phase of two voxels that are at a Euclidean distance r apart, as a function of r . As shown in the inset, it decays as a power law with slope 0.75 ± 0.02 .

ϕ_i of the voxels. We notice that this correlation function is usually studied in Ising-like spin models. We find that $C(r)$ decays algebraically with distance, as shown in Fig. S3, and follows a power law form, $C(r) \sim r^{0.75}$. The value of the exponent 0.75 ± 0.02 was calculated through standard OLS regression. Notice that this function does not go to 0 asymptotically, but reaches a value of 0.1, which represents the average correlation (notice that in the definition of the correlation, the average value was not subtracted). This indicates that long-range correlations remain strong even at large distances. Further analysis is required to elaborate on this point, which is currently outside the scope of our present study.

VI. EXPONENTS CALCULATION

In Fig. 2D of the main text we show an aggregate average of the degree distributions for all clusters. This curve exhibits the general trends of the $P(k)$ distribution, demonstrating for example the heavy tail, but it cannot be used for a direct determination of the exponent γ .

In our work we studied the properties of 192 network clusters, as described in the main text. The calculation of the scaling exponents was done separately for each network. The resulting set of 192 values was then analyzed through non-parametric boot strap analysis, in order to get the average value of the exponent and the corresponding confidence intervals.

As an example, in Fig. S4 we show the degree distributions for 9 different clusters. In the plots, it is clear that there is always a plateau at small k values, while in many cases there is an asymptotic exponential cutoff. We fitted these distributions assuming that a power law describes the data within a given interval only. For this, we used a generalized power-law form

$$P(k; k_{min}, k_{max}) = \frac{k^{-\gamma}}{\zeta(\gamma, k_{min}) - \zeta(\gamma, k_{max})}, \quad (10)$$

where k_{min} and k_{max} are the boundaries of the fitting interval and the Hurwitz ζ function is given by $\zeta(\gamma, \alpha) = \sum_i (i + \alpha)^{-\gamma}$.

We used the maximum likelihood method, following e.g. Clauset et al, SIAM Review, 51, 661 (2009). The fit was done in an interval where the lower boundary was k_{min} . For a given k_{min} value we were fixing the upper boundary to $k_{max} = wk_{min}$, where w is a parameter. We calculated the slopes in successive intervals by continuously increasing k_{min} and varying the value of w from 4 to 30. In this way, we sampled a large number of possible intervals. For each one of them we calculated the maximum likelihood estimator through the numerical solution of

$$\gamma = \operatorname{argmax} \left(-\gamma \sum_{i=1}^N \ln k_i - N \ln [\zeta(\gamma, k_{min}) - \zeta(\gamma, k_{max})] \right) \quad (11)$$

where k_i are all the degrees that fall within the fitting interval and N is the total number of nodes with degrees in this interval. The optimum interval was determined through the Kolmogorov-Smirnov test.

For the goodness-of-fit test, we used the Monte-Carlo method described in Clauset et al. For each possible fitting interval we generated 10000 synthetic random distributions following the best-fit power law. We then calculated the value of the Kolmogorov-Smirnov (KS) test for each one of them and measured the fraction p_{fit} of realizations where the real data KS value was smaller than the synthetic SK value. We accepted the power-law hypothesis when this ratio was larger than $p_{fit} > 0.2$. The average ratio over all clusters that were retained was $p_{fit} = 0.65$. In this way, it is possible that we could accept more than one exponents for a given cluster at different intervals. In all these cases, the different γ values were very close to each other and we considered the final exponent to be the average of the individual exponents.

Standard boot strap analysis on the resulting set of the individual cluster values yielded the exponent $\gamma = 2.11 \pm 0.04$, with a 95% confidence interval [2.039, 2.178].

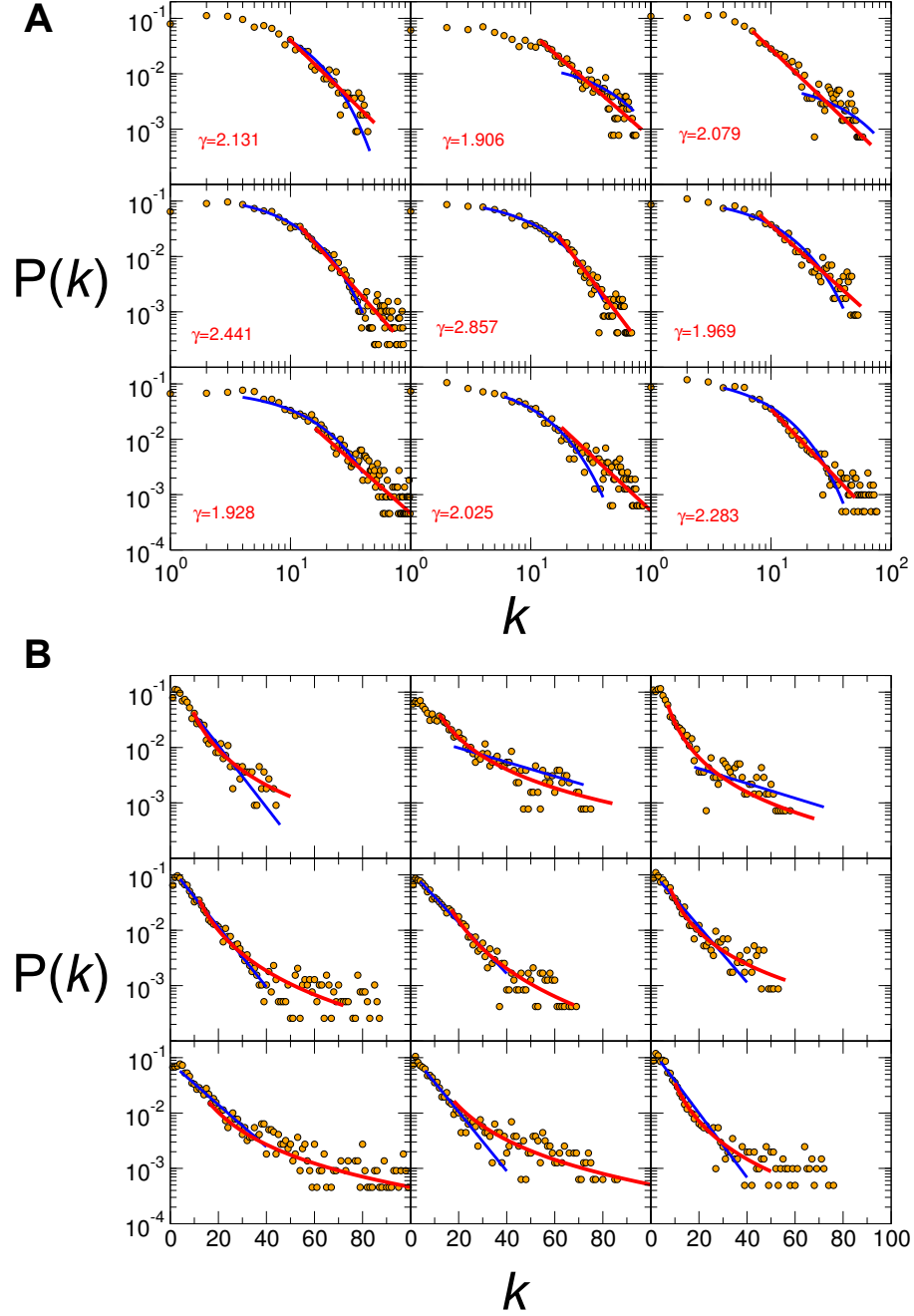


FIG. S4. **Degree distribution for network clusters.** A number of degree distribution functions $P(k)$ are shown for different clusters. The red lines correspond to the best power-law fitting, and the blue ones to an exponential fitting. **(A)** Degree distribution $P(k)$ in logarithmic axes. The power-law slopes correspond to the exponent γ , and are shown on the plots. **(B)** The same distributions and fittings in semi-logarithmic axes.

The same analysis was performed to test for a possible exponential description of the data. We scanned the same intervals as for the case of power-law and we used the maximum likelihood method to determine the optimum exponential fitting to the form:

$$P(k; k_{min}, k_{max}) = \frac{1 - e^{-\lambda}}{e^{-\lambda k_{min}} - e^{-\lambda k_{max}}} e^{-\lambda k}. \quad (12)$$

We again used KS statistics to determine the optimum fitting intervals and also the goodness-of-fit. In all the cases where the power-law was accepted, the exponential fitting gave an average ratio of $p_{fit} = 0.017$, which rules out the possibility of an exponential distribution.

VII. SCALING ANALYSIS

The structure of a fractal network can be characterized by a set of scaling exponents. They define the scaling of many important system properties. Some of these properties and the corresponding exponents are as follows:

- a. The degree distribution: $P(k) \sim k^{-\gamma}$, where γ is the degree exponent [44].
- b. The scaling of the mass with size: $N_B \sim \ell_B^{-d_B}$, which defines the fractal exponent d_B [22].
- c. The degree-degree distribution $P(k_1, k_2) \sim k_1^{-\gamma+1} k_2^{-\epsilon}$, where ϵ is the degree-degree exponent, and can be measured through $E_b(k) \sim k^\epsilon$, which is the integration of $P(k_1, k_2)$ over k_2 [48].
- d. The probability that modules are connected through their hubs, $\mathcal{E} \sim \ell_B^{-d_e}$ defines the hub-hub exponent d_e [23].
- e. The scaling of the degree of the modules with the size of the modules: $s \sim \ell_B^{-d_k}$, which defines the d_k exponent [22].
- f. The scaling of the modular factor as defined in Eq. (3): $\mathcal{Q}(\ell_B) \sim \ell_B^{d_M}$, through the modularity exponent d_M [27,28].

Scaling theory then defines precise relations between the exponents valid for fractal scale-free networks:

- g. $\gamma = 1 + d_B/d_k$ [22],
- h. $\epsilon = 2 + d_e/d_k$ [48], and
- i. $d_M = d_B - d_x$ [27,28].

We have measured directly all the exponents (see Fig. 2 and Fig. S5) for the brain modules

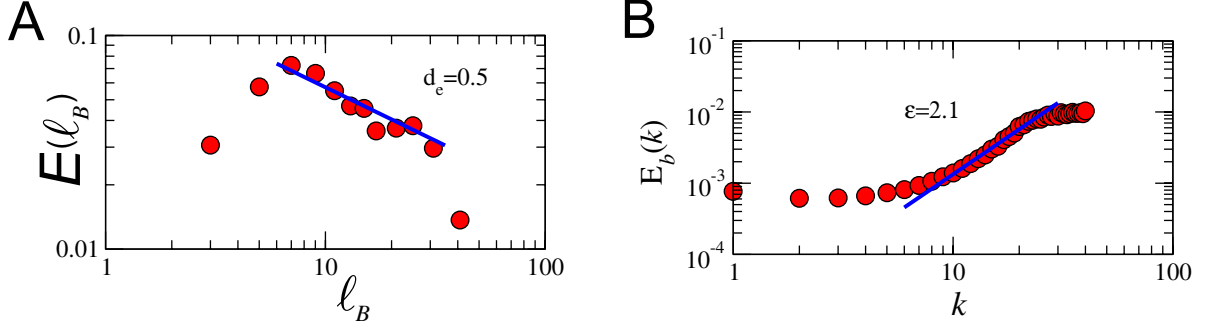


FIG. S5. **Calculation of the scaling exponents.** **(A)** Hub-hub exponent d_e through the scaling of $\mathcal{E}(\ell_B)$. **(B)** Degree-degree exponent ϵ through the dependence of $E_b(k)$ on the degree k [48].

and find: $\gamma = 2.11 \pm 0.04$, $d_e = 0.51 \pm 0.08$, $d_B = 1.9 \pm 0.1$, $d_k = 1.5 \pm 0.1$, $\epsilon = 2.1 \pm 0.1$, $d_M = 1.9 \pm 0.1$. Using these values in the known scaling relations above (g) and (h), we predict $\gamma = 2.26 \pm 0.11$ and $\epsilon = 2.34 \pm 0.06$, which are reasonably close to the calculated exponents $\gamma = 2.11$ and $\epsilon = 2.1$ from the direct measures. This set of results gives support to a scale-free fractal morphology of the brain modules. Notice that a Euclidean 2d lattice would be obtained in the limit $\gamma \rightarrow \infty$, $d_k=0$, $\epsilon \rightarrow \infty$.

VIII. MODULARITY ANALYSIS

In the main text of the paper we have described our modularity analysis of the brain clusters according to the MEMB technique. The modular properties of the same clusters can be also analyzed through techniques that partition a network according to maximization of modularity. We employed the Girvan-Newman method [20], which locates the point where the modularity measure, Q , is maximum. The definition of Q according to [20] is:

$$Q = \sum_{i=1}^{N_M} \left(\frac{l_i}{L} - \left(\frac{d_i}{2L} \right)^2 \right), \quad (13)$$

where N_M is the number of modules, L is the number of links in the network, l_i is the number of links within the module i , and d_i is the sum of the degrees in this module. A value of $Q = 0$ corresponds to a completely random configuration or to the case of one module only.

For the brain clusters we found an average modularity value of $Q = 0.82$. This is an indication of strong modularity within each cluster. A direct comparison between MEMB

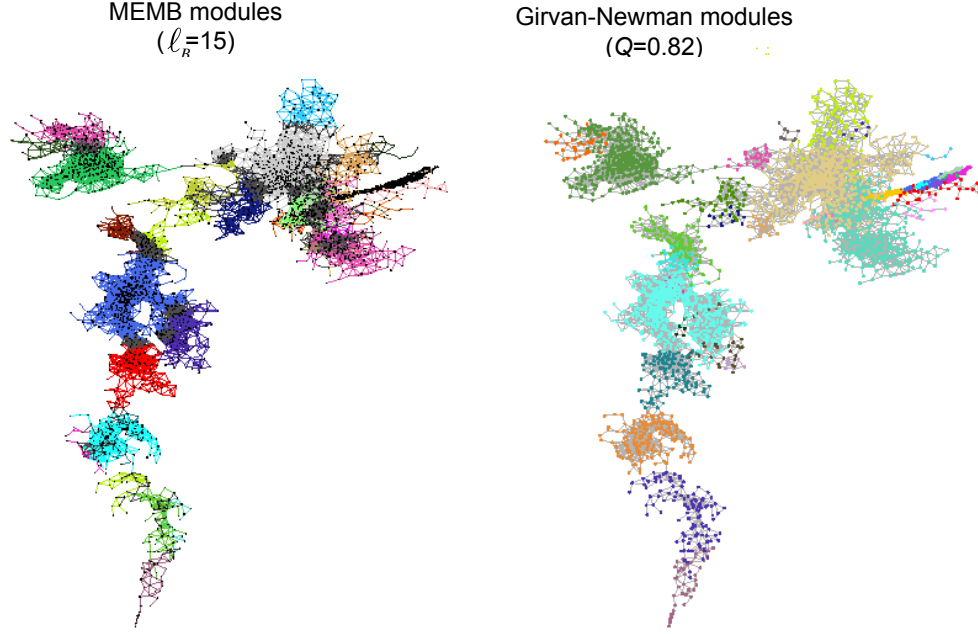


FIG. S6. **Modular properties of the brain clusters.** Comparison between the partition provided by the MEMB method (at $\ell_B = 15$) with the corresponding partition using the Girvan-Newman method [20]. The modularity index from the Newman definition Q is around 0.82, as found by the latter method. Both methods yield similar sub-modules.

and the Girvan-Newman method shows that they result in quite similar partitions. We calculated that 92% of the total links belong within a given module in both methods. A visual comparison is shown in Fig. S6. The maximization of modularity verifies the modular character of the clusters. The use of the MEMB, though, provides us with the extra advantage of modifying the scale at which we observe the modules to determine whether the modular structure is scale-invariant, i.e., if it is composed of modules inside modules.

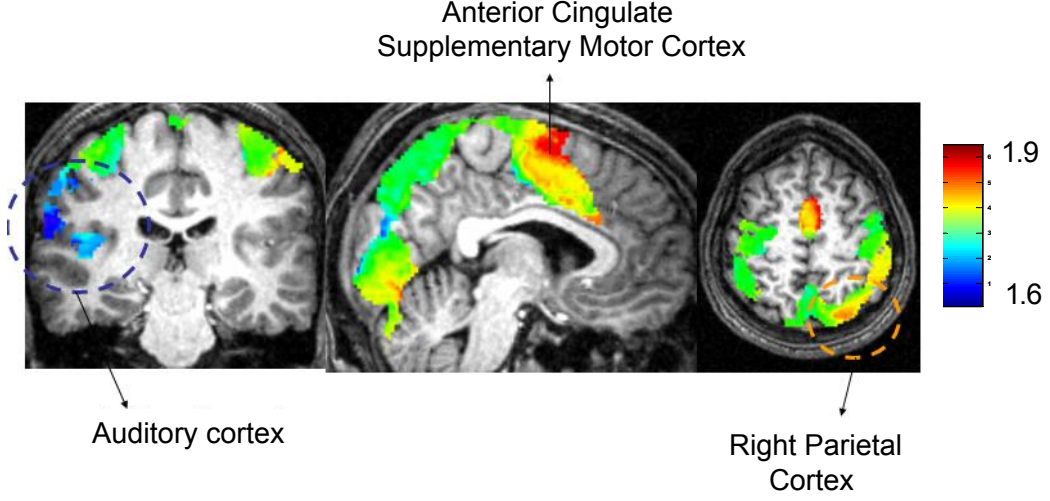


FIG. S7. **Topographical map of module fractality.** For each voxel, we calculate the average fractal dimension of the clusters to which it belongs, considering only voxels which form part of a cluster for at least eight subjects, to assure that mean values are not heavily determined by individual contributions. While the average over all clusters is $d_B = 1.9 \pm 0.1$, the dimension of each cluster exhibits small variations around this value which allows us to identify consistent differences among them. The clusters in the auditory cortex present the smaller fractal dimension d_B , while parietal and motor clusters show intermediate values of d_B . The right portion of the SMA and the right PPC were the clusters with the higher fractal dimension.